

High Speed Synchrotron X-ray Imaging Studies of the Ultrasound Shockwave and Enhanced Flow during Metal Solidification Processes

D. Tan¹, T. L. Lee¹, J. C. Khong¹, T. Connolley², K. Fezzaa³, J. Mi^{1*}

¹University of Hull, Cottingham Road, Hull, East Yorkshire, HU6 7RX, UK

²Diamond Light Source, Didcot, Oxfordshire, OX11 0DE, UK

³Advanced Photon Source, Argonne National Laboratory, Argonne, Illinois 60439, USA

Abstract

The highly dynamic behaviour of ultrasonic bubble implosion in liquid metal, the multiphase liquid metal flow containing bubbles and particles, and the interaction between ultrasonic waves and semisolid phases during solidification of metal were studied *in situ* using the complementary ultrafast and high speed synchrotron X-ray imaging facilities housed respectively at the Advanced Photon Source, Argonne National Laboratory, US, and Diamond Light Source, UK. Real-time ultrafast X-ray imaging of 135,780 frames per second (fps) revealed that ultrasonic bubble implosion in a liquid Bi-8 wt. %Zn alloy can occur in a single wave period (30 kHz), and the effective region affected by the shockwave at implosion was 3.5 times the original bubble diameter. Furthermore, ultrasound bubbles in liquid metal move faster than the primary particles, and the velocity of bubbles is 70 ~ 100% higher than that of the primary particles present in the same locations close to the sonotrode. Ultrasound waves can very effectively create a strong swirling flow in a semisolid melt in less than one second. The energetic flow can detach solid particles from the liquid-solid interface and redistribute them back into the bulk liquid very effectively.

- The corresponding author: J.Mi, Email: j.mi@hull.ac.uk, Tel: +44 01482 465670

Introduction

The transmission and attenuation of ultrasonic waves in a solid medium and its interactions with the constituents inside solids are well understood, for example, ultrasound attenuation in steels [1] and its synthetic effects on inorganic materials and metal powders [2, 3]. Based on those well-developed theories, ultrasound-based imaging, non-destructive testing techniques and the relevant instruments have been well developed and widely used in industry [4 - 7]. Similarly, theories regarding the propagation of ultrasonic waves in a single phase liquid medium are also well developed. Above a certain acoustic pressure threshold – the Blake's threshold [8], ultrasound can generate bubbles in a liquid medium. The bubbles, driven by the alternating acoustic pressure field in the liquid, can oscillate, grow, coalesce, and split, and under certain conditions collapse violently. This is a process commonly known as ultrasonic cavitation and bubble implosion [9]. Previous studies in the field of sonochemistry [10 - 13] revealed that bubble implosion can generate a shockwave with an extremely high pressure (>1000 atm) and temperature (>5000 K) immediately adjacent to the bubble surface, leading to complicated sonochemical reactions. Ohl and Ikink [14] also reported that, when bubble implosion occurs near a rigid interface, microjets with extremely high velocity can be created near the interface. However, those studies were mainly carried out in light-transparent liquid media, such as water or water based solutions [9, 15]. The dynamic behaviour of cavitation bubbles during coalescence and splitting, especially at the instant of bubble implosion has not been fully understood, because of the highly transient nature of cavitation, and the difficulties in developing a predictive model to describe precisely the underlying governing physics [10].

A few attempts have been made using synchrotron X-ray imaging techniques to study ultrasound bubbles *in situ* and in real-time [16], including the dynamics of bubble oscillation and bubble implosion in opaque materials such as liquid metals [17, 18]. One of the driving forces for such studies is to understand the precise mechanism of how the solidification microstructure of metal alloys, regardless of the alloy chemistry, is refined by applying ultrasonic waves into metal alloys during the solidification process. Laboratory-based research in this field started in 1930s, and a wide range of fundamental and applied research on ultrasonic processing of metal alloys were conducted in Russia from the 1960s to the 1980s, which was well documented and reviewed in a new book by the Eskins [8].

In the past ten years or so, the global demand for developing and adopting environmental friendly and sustainable technologies for metal manufacturing has stimulated a worldwide resurgence in this research field. The effectiveness of degassing and grain refinement using ultrasound has been demonstrated in several alloy systems, including Al [19, 24], Mg [20, 21], Sn [22], and Fe [23] based alloys. Generally, three mechanisms have been proposed for the underlying physics of grain refinement: (1) the enhancement of homogeneous nucleation because of bubble implosion induced high pressure, which effectively increases the melting point of the metal alloy at the region very close to the bubble and therefore increase the level of undercooling for nucleation [25, 26]; (2) the activation of potential inoculating particles for heterogeneous nucleation [8, 23], and (3) grain multiplication due to dendrite fragmentation [27 - 30]. However, almost all previous research has been based on post-mortem microstructure analysis made on the solidified samples, linking the results to the ultrasound parameters applied, including ultrasound power, frequency, duration, the melt temperature, etc. There have been hardly any systematic studies using *in situ* observation of the real-time dynamic interactions between ultrasound bubbles and the liquid and solid phases, apart from very limited work on organic-transparent alloys [28, 30]. Hence the relative importance of the above grain refinement mechanisms has never been fully clarified, and the industrial uptake of this technology is therefore stalled.

In this paper, we used high speed synchrotron X-ray imaging techniques to study *in situ* the highly dynamic behaviour of bubble implosion in liquid metal, the enhanced metal flow due to ultrasonic waves, and the interaction between the metal flow and semisolid phases during the solidification process. Information was extracted from the real-time image sequences to provide quantitative information on the key mechanisms that govern ultrasound induced grain refinement in metallic systems.

Experiment

Ultrafast and high speed synchrotron X-ray imaging beamlines

The ultrafast and high speed synchrotron X-ray imaging experiments were conducted at sector 32-ID-B of the Advanced Photon Source (APS), Argonne National Laboratory, US and the Joint

Environmental, Engineering and Processing (JEEP) beamline (I12) of Diamond Light Source (DLS), UK.

At APS, the storage ring has a circumference of 1104 m and is filled with 7 GeV electrons from the booster. It provides, in the western hemisphere, the brightest synchrotron X-ray beam with a peak irradiance of 10^{14} photon/s/mm²/0.1%bw [31]. The storage ring can be operated in a hybrid filling mode, in which most of the electron current is stored in the “long” electron bunch that generates a 500 ns X-ray pulse with an intensity 6 times higher than that obtained in the uniform filling mode [31, 32]. Sector 32-ID-B is a dedicated undulator source designed to fully utilise the 500 ns X-ray pulse by synchronizing the X-ray pulse from the storage ring with the ultrafast shutter and the camera on the beamline. The 500 ns X-ray pulse is circulating in the storage ring and comes around in every 3.68 μ s, delivering an effective image acquisition rate of up to 271,554 fps with a spatial resolution of 1 μ m/pixel dependant on the field of view. The synchronization ensures that the image of an object is taken within the 500 ns exposure time, providing an image temporal resolution of \sim 500 ns regardless of the frame acquisition rate. This is the highest among the Synchrotron X-ray based imaging beamlines around the world, only inferior to the X-ray free electron laser based imaging technique, such as those available at the Linac Coherent Light Source at Stanford University [33, 34].

DLS, the UK’s national synchrotron light source, has a 3 GeV electron storage ring with a circumference of 562 m. The I12 JEEP beamline is a dedicated high energy instrument on a 4.2 T wiggler source, offering white or monochromatic X-ray beams between 50 and 150 keV for imaging, diffraction and tomography experiments. I12 has a large beam size (up to 50 mm \times 12 mm in Experimental Hutch 1) and an X-ray imaging system with interchangeable objective lenses. The imaging system allows users to automatically select different image magnifications and hence fields of view. (We typically chose a field of view of 6.6 \times 5.4 mm with a spatial resolution of 12.2 μ m/pixel versus the 1 \times 1 mm with a spatial resolution of 1 μ m/pixel at 32-ID-B of APS). The wider field of view on I12 is therefore suitable for studying the collective behaviour of bubble clouds and their interactions with the metal flow and semisolid phases. Feasible acquisition speeds are dependent on sample attenuation and region of interest cropping. In our experiments we used up to 2000 fps with filtered white beam (fixed filtration of 2.2 mm diamond, 5.5 mm SiC, and optional filtration of 6 mm Cu plate).

The experimental apparatus and the set up at the beamlines

Fig. 1(a) is a photo showing the experimental apparatus and the set up at 32-ID-B of APS. A similar set up was used at I12 JEEP of DLS. The custom-made experimental apparatus has two key elements: (1) a specially-made furnace and a purposely-designed quartz tube container for melting and holding metal alloys; and (2) an ultrasound processor (UP100H from Hielscher) and a sonotrode to transmit ultrasonic waves into the metal alloys held inside the quartz tubes.

The furnace consists of four plates made from machinable ceramic (Duratec 750), including 1 front plate and 1 back plate with the same dimension of 120 mm (width) \times 120 mm (height) \times 20 mm (thickness); and 2 side plates with the same dimension of 35 mm (width) \times 120 mm (height) \times 20 mm (thickness). Holes of 10 mm in diameter were drilled through the thickness of the plates to accommodate six cartridge heaters with 2 seated inside the front plate, 2 inside the back plate, and 1 inside each of the side plates. Each cartridge heater is 9 mm in diameter and 52 mm long with a heating power of 300 W. The plates can be flexibly assembled around the quartz tube to form a rectangular enclosure to act as a furnace (Fig. 1(a) and 1(c)). The six cartridge heaters can deliver a heat power of 1.8 kW and heat the samples to 1073 K without difficulty. Windows of 5 mm (width) \times 30 mm (length) were machined along the central symmetrical lines of the front and back plates to allow X-ray to pass through the furnace and onto the thin channel area (\sim 300 μ m thick) of the quartz tube (Fig. 1(c)) which was made using the following procedure. Firstly, two rectangular thin quartz sheets (15 \times 10 \times 1.2 mm) were put in parallel together with a gap of \sim 300 μ m in between. Secondly, the edges along the 10 mm side of the two sheets were welded together using a gas torch to form the thin channel of \sim 300 μ m internal gap. Finally, the two openings of the thin channel along the 15 mm side were linked and welded onto two 40 mm long quartz tubes (13 mm outside diameter and 1.5 mm wall thickness from Robson ScientificTM). Careful operations were carried out in the quartz softening temperature range to deform one end of the quartz tubes into a wedge-shaped transition area in order to fit smoothly and then welded together with the thin channel. The photos in Fig. 1(c) show the typical quartz tubes with the thin channel in the middle which were all made in the Glass Workshop housed at the Department of Chemistry, University of Hull. The \sim 300 μ m internal gap in the thin channel area is wide enough to allow the ultrasonic bubbles generated immediately under the sonotrode tip (Fig. 1(c)) to pass

through the channel, while thin enough to allow X-rays to penetrate the metal alloy held inside the channel with enough photon flux to form images at an acquisition rate of up to 271,554 fps.

A Bi – 8 wt. % Zn alloy that made from high purity elemental Bi (99.999%) and Zn (99.99%) was used in the experiment. The phase diagram of Bi-Zn system can be found in Fig.2. The alloy was chosen because of its low melting temperature, and the adequate X-ray absorption contrast between Bi and Zn for high speed synchrotron X-ray imaging. Three 250 μm diameter K-type thermocouples were placed at the top (TC1), middle (TC2) and bottom (TC3) positions inside the thin channel (Fig. 1(c)) to monitor and record the temperatures of the alloys during melting and cooling operations. The desired temperature gradient in the alloy inside the thin channel was controlled by (1) adjusting the position of the quartz tube relative to the cartridge heaters, and (2) placing a cold brass rod ($\phi 9 \times 15$ mm) below the thin channel to act as a heat sink (Fig. 1(c)). By imposing a suitable temperature gradient, a clear liquid-to-solid transition zone can be purposely created in the middle of the thin channel, for example, at the location around TC2 as shown later in Fig. 6, allowing the characteristics and the growth of a liquid-solid (L-S) interface and its interactions with the ultrasonic bubbles and the enhanced flow to be studied *in situ*.

An UP100H ultrasound processor (Fig. 1(a)) made by HielscherTM was used in the experiment. It has a fixed frequency of 30 kHz, and adjustable input power of 0 – 100 W with a maximum acoustic power density of 600 W/cm². Sonotrodes of 74 mm long with a tip diameter of either 0.3 or 2 mm were used and positioned at the wedge area above the thin channel to transmit ultrasonic waves into the liquid metal held inside the thin channel. The ultrasound processor was mounted on a precision linear stage, and its vertical movement was independent from that of the sample stage, facilitating imaging with X-rays either at the tip of the sonotrodes or at the area of interest within the thin channel. The on/off switching and the duration of the applied ultrasonic waves were controlled by a custom-designed relay apparatus, operated from outside the experimental hutch.

The experimental parameters for ultrafast and high speed imaging

At 32-ID-B of APS, a white beam with the undulator gaps set to 14 to 18 mm were used in the experiments, and it was found that the energy spectrum at 18 mm undulator gap (Fig. 1(b)) gave

the best images for majority of the liquid metal experiments. Most of the intensity at this gap is located within the first harmonic around 7.7 keV with the peak irradiance of 3.4×10^{14} photon/s/mm²/0.1%bw, and a natural bandwidth of 0.4 keV full-width at half-maximum. A fast mechanical shutter is placed at the upstream of the X-ray beam path to manage the intense heat load generated by the white beam, allowing only a few tens of ms exposure of white beam onto the samples when acquiring images so as to avoid overheating the samples [31]. The images sequences were acquired using a Photron FASTCAM SA1.1 camera (Fig. 1(a)) optically coupled to a fast scintillator crystal (LYSO:Ce). The sample-to-detector distance was set at 980 mm (Fig. 1(c)). The ultrafast image acquisition capability allows the highly dynamic behaviour of ultrasonic bubbles to be studied with a spatial resolution of 1µm/pixel in the viewing fields of 1024 × 1024 µm at 5413 fps, and 258 × 198 µm at 135,780 fps. The viewing field becomes smaller when higher image acquisition rate is used due to the limited readout speed of the camera.

At I12 JEEP on DLS, a white beam was used. In addition to the fixed filters along the X-ray path, 6 mm thick Cu filters (2 mm + 4 mm) were added upstream to manage the heat load, allowing longer exposure times to be used without heating and damaging the samples [37]. Images were taken using a 700 µm thick Lutetium Aluminium Garnet detector, doped with Cerium (LuAG:Ce), and recorded using a Vision Research Phantom™ V7.3 high speed camera. The sample-to-detector distance was set at 900 mm. The flexible swap between different view fields (from 23 mm × 12 mm to 1.8 mm × 1.3 mm with a spatial resolution from 29.7 to 2.2 µm/pixel) at JEEP made it possible to study the behaviour of fluid flow and their interactions with the solid and semisolid phases during solidification.

Results and discussions

Image acquisition, processing and analysis

Fig. 3(a) shows a typical raw image extracted from an image sequence acquired at APS using 5413 fps. Before any meaningful image processing, the features visible in the raw image are often not very clear due to noise from the scintillator, camera, and the non-uniform distribution of X-ray beam intensity in the imaged area.

We therefore used the relevant functions available in the Matlab[®] image processing toolbox to process the images. Firstly, a clear and uniform background image obtained from a pure liquid (Fig. 3(b)) was subtracted from the raw image (Fig. 3(a)). The image artefacts caused by the defects on the scintillator, or strip noises due to the camera operated at high frame rate were therefore removed or minimized so as to reveal the real features more clearly (Fig. 3(c)). Secondly, the build-in band-pass filter in Matlab[®] [38] was applied to Fig. 3(c) to enhance the contrast (Fig. 3(d)). Finally a binary operation was applied on Fig. 3(d) to clearly segment the bubbles and particles (Fig. 3(e)) for any further statistical analysis. To maintain consistency, the same image processing parameters, e.g. the minimum and maximum grey scales and frequency, were used for all images in the same image sequence.

We also developed a Matlab[®] program to extract the time-resolved information of every bubble and particle in the image sequence, e.g. the shape and centre location (Fig. 3(f)), trajectory and velocity of each bubble and particle. For example, five particles marked P1, P2, P3, P4 and P5 in Fig. 3(e) were selected, and their trajectories were calculated using the standard 4 frame tracking algorithm [39] based on the time-resolved locations of the target objects in the consecutive images by estimating their most probable path and plotted in Fig. 3(g). The bubbles or particles velocities can be calculated by using the translation distance over the time interval between the consecutive images. However, any movement in the thickness direction cannot be obtained because of the nature of the 2D images. Actually the geometrical design of the thin channel ensured that the ultrasound wave and the associated fluid moved downwards without any noticeable movement in the thickness direction, therefore the relative movement of the particles and the bubbles in the thickness direction can be ignored in this case.

Bubble implosion and shockwave in liquid metal

Fig. 4(a) – (f) show six images in a single wave period (33.3 μ s for the 30 kHz ultrasonic wave) extracted from an image sequence captured at APS using 135,780fps in a liquid Bi – 8 wt. %Zn alloy at 700 K. The temperature was measured by TC1, immediately below the sonotrode tip. In this case, a 2 mm diameter tip sonotrode and an input ultrasound power of 20 W were used. At this ultrafast image acquisition rate, the up-and-down cyclic movement of the sonotrode tip in a single wave period can be clearly tracked and then linked to the corresponding acoustic pressure

as showed in details in Fig. 4(g). The sonotrode tip position (black square in Fig. 4(g)) measured from each image followed exactly the sine wave of the ultrasound.

Fig. 4(a) – (c) show that, during the upwards half cycle, the sonotrode tip moved from position a to b and then to c (Fig. 4(g)). The corresponding acoustic pressure decreased from near the maximum positive pressure to near the maximum negative pressure (Fig. 4(g)). As the result, a bubble of $\sim 12 \mu\text{m}$ in radius (Fig. 4(b)) grew to $\sim 23 \mu\text{m}$ in radius in $7.4 \mu\text{s}$ (Fig. 4(c)).

After reaching the highest position (position c in Fig. 4(g)), the sonotrode started the downwards half cycle, and the acoustic pressure increased and compressed the bubble in Fig. 4(c) to a radius of $\sim 19 \mu\text{m}$ in $7.4 \mu\text{s}$ (Fig. 4(d)). As the sonotrode reached almost the lowest position, the maximum compressive acoustic pressure was reached, forcing the bubble to implode violently and forming a blurred-and-misty circular region as shown in Fig. 4(e). In the next image (Fig. 4(f)), i.e. $7.4 \mu\text{s}$ after the implosion, no residual “debris” or tiny bubbles were observed, again most likely because of the limitation of the spatial resolution.

Fig. 4(h) shows two curves, d-d and e-e, representing the counts of grey level for the dash lines marked d-d in Fig. 4(d) and e-e in Fig. 4(e). The curve d-d clearly shows that, for the bubble in Fig. 4(d), there is a relatively constant but higher grey value (~ 250) region in the center, representing the main body of the bubble filled most likely with any diffused gas from the liquid metal. The two regions with a steep change of grey value on either side the curve d-d represented the boundary of the bubble, and actually it was the bubble wall separating the liquid metal and the gas trapped inside the bubble. Therefore, the distance marked as A ($\sim 38 \mu\text{m}$) was actually the diameter of the bubble in Fig. 4(d).

In contrast, the blurred-and-misty circular region in Fig. 4(e) did not have such a distinct bubble wall. The curve e-e in Fig. 4(h) shows that, there was a relatively high grey value (~ 225) area in the center marked by C with a distance of $\sim 17 \mu\text{m}$; and outside C the grey values followed gradually reduced slopes. Again, using the Gilmore model [18], the bubble diameter instantly before the bubble implosion is estimated at $20 \mu\text{m}$, which is very close to measured distance C in Fig. 4(h). More interestingly, the tiny peak of the grey value pointed by the blue arrow also indicated that there could be tiny bubble debris or a new nucleus present at the center due to the implosion.

Apparently, the grey values of the curve e-e outside distance C were higher than that of the liquid metal, but lower than that of the bubble, indicating that there was a gradual change of X-ray absorption capability (a gradual change of materials density) for the materials along the area delineated by line e-e. This phenomenon is most likely caused by the shockwave produced at bubble implosion as explained below. The pressure created by the shockwave at the bubble wall expelled the gas trapped inside the original bubble into the nearby liquid and formed a gas-liquid mixture with its density lower than that of the liquid metal but higher than that of the gas originally trapped inside the bubble. The gas-liquid mixture region was actually reflected in X-ray image as the blurred-and-misty circular region showed in Fig. 4(e) which spanned from an initial diameter of $\sim 17 \mu\text{m}$ to $\sim 60 \mu\text{m}$ as marked by B in the curve e-e in Fig. 4(h). Clearly, in this case, B represented the upper limit of the region which the bubble implosion (shockwave) reached, which is about 3.5 times the diameter of the bubble immediately before implosion. The *in situ* imaging study also confirmed that bubble implosion in liquid metal can occur in a single wave period.

Multiphase flow under ultrasonic waves

Ultrasonic bubbles are often created collectively in a condition where the critical acoustic pressure threshold is exceeded [8]. Their dynamic interaction with the liquid metal and any primary particles in the liquid metal are very important for understanding the ultrasound processing of liquid metals [2, 3]. Fig. 5(a) – (c) show a series of image sequences captured at APS using 5413 fps at 0.5, 2.5, and 4.5 mm below the sonotrode tip, respectively. The melt temperatures measured at TC1, TC2 and TC3 were 650 K, 630K, 600K respectively, indicating that the alloy was in a fully liquid state. A sonotrode with a tip diameter of $\sim 0.3 \text{ mm}$ and 20 W input power were used in the experiment to allow the dynamic behaviour of bubbles and particles surrounding the sonotrode tip to be imaged within the limited field of view, i.e. $1 \text{ mm} \times 1 \text{ mm}$ at 5413 fps. Fig. 5(a-1) shows that, although the alloy is in a liquid state, some solid Zn particles (pointed by the arrows in Fig. 5(a-1)) formed around the sonotrode tip because of the relatively cold surface of the sonotrode tip. After applying ultrasound of 20 W, the Zn particles were “shaken” off the tip and flew downward together with any ultrasound bubbles as shown in Fig. 5(a-2) - (a-4). Due to the limited field of view ($1 \times 1 \text{ mm}$ in this case), the behaviours of the bubbles and particles further away from the sonotrode tip were imaged separately using the

identical melt conditions and ultrasound input power as that in Fig. 5(a). The typical image sequences captured at 2.5 mm and 4.5 mm below the sonotrode tip are shown in Fig. 5(b) and 5(c), respectively. The image sequences taken at the different distances away from the sonotrode tip allowed systematic and statistical datasets to be extracted from the images for studying quantitatively the dynamic behaviours of the bubbles, the particles and the enhanced metal flow under ultrasonic waves.

Firstly, the dynamic behaviours of an individual bubble and a particle were studied in detail by extracting 8 images that contained a typical bubble and a typical Zn particle from the Fig. 5(b) image sequence. The 8 selected images were enlarged and shown in Fig. 5(d) with the bubble circled and marked B, and the particle boxed and marked P. Using the in-house Matlab[®] code, the movement of B and P were tracked and their velocities were calculated and showed in Fig. 5(e). Clearly, B moved in a zigzag manner, while P travelled in a straight line, and the calculated average velocity of B (0.26 m/s) was ~70% higher than that of P (0.15 m/s). These results indicate that the alternating acoustic pressure affects much more the movement of bubbles than that of the particle. Statistical analyses made on all the images and videos studied revealed that the trajectories of the particles were either a straight line (Fig. 5(e)), or slightly curved paths (Fig. 3(g)), further confirming that the particles are mainly dragged and moved by the flow of liquid metal, but not affected much by the alternating acoustic field.

To study the effect of ultrasound power on the multiphase flow, a new sample was studied using an ultrasound input power of 60 W with all other experimental conditions unchanged (the same alloys, temperatures, and beam conditions), and the results were compared with those obtained from the case with 20 W ultrasound input powder. Fig. 5(f) summarises the calculated velocities for the particles and bubbles in the images (> 20 particles and bubbles were measured in each image sequence) captured at different locations below the sonotrode tip with the ultrasound input powers of 20 and 60 W, respectively. The results show that the applied ultrasound power is one of the dominant control parameters for the multiphase liquid metal flow containing bubbles and particles. Both bubble and particle velocities increase with the increase of ultrasound power and decrease at locations further away from the sonotrode tip. In all cases, the bubble velocity is 70 - 100% higher than the particle velocity at the location close to the sonotrode tip, but the difference in velocity reduces gradually as it moves away from the sonotrode tip.

After studying and understanding the highly dynamic behaviour of bubbles and particles using the ultrafast X-ray imaging capability at 32-ID-B of APS, we used the relatively slow speed (~ 1500 fps), but larger viewing field imaging system available at I12 JEEP of DLS to study the interaction between the ultrasound enhanced fluid flow and the L-S interface during the solidification process. By carefully controlling a temperature gradient of ~ 3.9 K/mm for the liquid held inside the thin channel, and imposing a constant cooling rate of 0.2 K/s, the liquid metal was cooled to the semisolid temperature range with an L-S interface clearly formed near the central region of the thin channel. Fig. 6(a-1) - (a-6) are the typical images captured at the location ~ 4.5 mm below the sonotrode using 1500 fps (an exposure time of $660 \mu\text{s}$) at DLS. A sonotrode with a 2 mm diameter tip and an ultrasound input power of 60 W were used. The temperature measured at TC2 (the center of the images) was 540 K. Fig. 6(a-1) shows that, before applying ultrasound, the white Zn particles accounted for $\sim 40\%$ of the area below the L-S interface in the viewing field. When ultrasound of 60 W input power was applied, a liquid jet flow was created and shot down from the central region of the viewing field, expelling and dispersing the Zn particles around, and forming a swirling flow at either side of the central line of the image, that is, clockwise direction on the left and anti-clockwise direction on the right (Fig. 6(a-2) – (a-4)). As the ultrasound continued, the Zn particles close to the L-S interface were “flushed” away gradually by the swirling flow at either side. After 1 s (the preset time to stop the ultrasound), a relatively stable and clear L-S interface was formed as shown in Fig. 6(a-5), because the majority of the loose Zn particles floating above the L-S interface were “washed” away, and replaced by a stream of clear liquid. Fig. 6(a-6) shows that, after the ultrasound was stopped, the detached Zn particles continued to move up with a speed of ~ 0.003 m/s driven by the residual swirling flow and the buoyancy force. The “washed” away Zn particles could act as the energy-favorable substrates for enhancing the nucleation of new grains in the bulk liquid.

Fig. 6(b) shows the flow velocity contour above the L-S interface when the fluid flow is stabilized after the application of ultrasound for 500 ms. This velocity contour was calculated based on the movement tracking of >100 particles of Zn in consecutive images of the image sequence. At 2.5 mm below the sonotrode (near the top of Fig. 6(a)), a maximum flow velocity of 0.25 m/s was established at the central region containing $\sim 40\%$ Zn particles (area fraction) in just 500 ms. In just 1000 ms ultrasound processing, nearly 50% of the Zn particles in the viewing field was washed away, with most of them being displaced within 500 ms (Fig. 6(a-3)), further

confirming that ultrasound enhanced fluid flow is very effective in dispersing and redistributing primary solid particles in the bulk liquid.

Previous studies argued that the increase in temperature due to the application of ultrasound also plays an important role in solute redistribution and remelting of any solid particles or dendritic grains [8]. Our study shows that applying ultrasound indeed increased the temperature of the liquid melt and the semisolid phases. Fig. 6(c) shows that initially the temperature difference between TC1 and TC2 was ~ 12 K, and it was reduced continuously when the ultrasound was applied until reached a relatively constant value of ~ 5 K after 1 s because the enhanced fluid flows transported hotter liquid from top (TC1) regions towards the L-S interface (TC2). However, the high speed image sequence shows that majority of the particles in the viewing field were detached or loose within 500 ms after applying ultrasound (Fig. 6(a-3)) during which there was hardly any obvious temperature increase (< 3 K) at the L-S interface region (TC 2 in Fig. 6(c)). Hence the hydrodynamic force induced by the enhanced fluid flow plays a more dominant role in dispersing and redistributing solid particles in the liquid metals.

Conclusion

Using the ultrafast synchrotron X-ray imaging facility at APS, the highly dynamic behaviour of ultrasound bubble implosion in liquid metal was captured and studied in real-time. Bubble implosion was found to occur in a single wave period (30 kHz), and the effective region affected by the shockwave at implosion was ~ 3.5 times of the original bubble diameter.

Ultrasound bubbles in liquid metal move faster than the primary particles, that is, 70 \sim 100% higher compared to the primary particles present in the same locations close to the sonotrode. However, the difference in velocity reduced significantly at the locations further away from the sonotrode tip.

Using the high speed Synchrotron X-ray imaging system with a relative large field of view at DLS I12, the ultrasound enhanced fluid flow in a semisolid condition (during solidification of metal) was studied *in situ*. The results show that the ultrasound enhanced swirling flow is a dominant mechanism to detach the solid particles from the liquid-solid interface in just a few

hundreds of milliseconds, redistributing them very effectively back into the bulk liquid with the possibility to act as the energy-favorable sites for nucleating new grains.

Acknowledgement

The authors would like to acknowledge the financial support from the U.K. Engineering and Physical Sciences Research Council (Grant No. EP/L019965/1), The Royal Society Industry Fellowship (for J Mi), and the Hull University & Chinese Scholarship Council (Hull-CSC) PhD Studentship (for D. Tan). The awards of the synchrotron X-ray beam time (EE8542-1) by the Diamond Light Source, UK, and the synchrotron X-ray beam time (GUP 23649 and GUP 26170) by the Advanced Photon Source, Argonne National Laboratory, US are also gratefully acknowledged. Use of the Advanced Photon Source, an Office of Science User Facility operated for the U.S. Department of Energy (DOE) Office of Science by Argonne National Laboratory, was supported by the U.S. DOE under Contract No. DE-AC02-06CH11357.

Special thanks also go to Julia Malle of Glass Workshop in the Department of Chemistry, University of Hull, who has assisted on making the special quartz tube containers used in the *in situ* synchrotron X-ray imaging studies.

References

1. R. L. Roderick and R. Truell: *J. Appl. Phys.*, 1952, vol. 23, pp. 267-79.
2. K. S. Suslick, D. J. Casadonte, M. L. Green and M. E. Thompson: *Ultrasonics*, 1987, vol. 25, pp. 56-59.
3. K. S. Suslick, S. Choe, A. A. Cichowlas and M. W. Grinstaff: *Nature*, 1991, vol. 353, pp. 414-16.
4. J. D. Achenbach and O. K. Parikh: *Rev. Prog. Q.*, Springer US, 1991, pp. 1837-44.
5. H. R. Mayer, H. Lipowsky, M. Papakyriacou, R. Rösch, A. Stich and S. Stanzl-tschegg: *Fatigue Fract. Eng. M.*, 1999, vol. 22, pp. 591-99.
6. D. G. Shchukin, E. Skorb, V. Belova and H. Möhwald: *Adv. Mater.*, 2011, vol. 23, pp. 1922-34.
7. J. Campbell: *Int. Mater. Rev.*, 1981, vol. 26, pp. 77-108.
8. G. I. Eskin and D. G. Eskin: *Ultrasonic Treatment of Light Alloy Melts*, 2nd ed., CRC Press, Boca Raton, Florida, US, 2015.
9. W. Lauterborn and T. Kurz: *Rep. Prog. Phys.*, 2010, vol. 73, pp. 1-88.
10. K. S. Suslick and D. J. Flannigan: *Annu. Rev. Phys. Chem.*, 2008, vol. 59, pp. 659-83.

11. M. L. Calvisi, O. Lindau, J. R. Blake and A. J. Szeri: *Phys. Fluids*, 2007, vol. 19, pp. 101-15.
12. D. J. Flannigan and K. S. Suslick: *Nature*, 2005, vol. 434, pp. 52-55.
13. K. S. Suslick, D. A. Hammerton and R. E. Cline: *J. Am. Chem. Soc.*, 1986, vol. 108, pp. 5641-42.
14. C. D. Ohl and R. Ikink: *Phys. Rev. Lett.*, 2003, vol. 90, pp. 21-24.
15. W. Lauterborn and C. D. Ohl: *Ultrason. Sonochem.*, 1997, vol. 4, pp. 65-75.
16. T. L. Lee, J. C. Khong, K. Fezzaa and J. Mi: *Mater. Sci. Forum*, 2013, vol. 765, pp. 190-94.
17. H. Huang, D. Shu, Y. Fu, J. Wang and B. Sun: *Ultrason. Sonochem.*, 2014, vol. 21, pp. 1275-78.
18. J. Mi, D. Tan and T. L. Lee: *Metall. and Mater. Trans. B*, 2014 (Open Access published online 11 Dec 2014), DOI: 10.1007/s11663-014-0256-z.
19. X. Jian, H. Xu, T. T. Meek and Q. Han: *Mater. Lett.*, 2005, vol. 59, pp. 190-93.
20. M. Qian and A. Ramirez: *J. Appl. Phys.*, 2009, vol. 105, pp. 81-86.
21. M. K. Aghayani and B. Niroumand: *J. Alloys Compd.*, 2011, vol. 509, pp. 114-22.
22. H. Chen, Z. Li, Z. Wu and Z. Zhang: *J. Alloys Compd.*, 2005, vol. 394, pp. 282-85.
23. O. V. Abramov: *Ultrasonics*, 1987, vol. 25, pp. 73-82.
24. T. V. Atamanenko, D. G. Eskin, L. Zhang and L. Katgerman: *Metall. Mater. Trans. A*, 2010, vol. 41, pp. 2056-66.
25. R. Hickling: *Nature*, 1965, vol. 206, pp. 915-17.
26. J. D. Hunt and K. A. Jackson: *J. Appl. Phys.*, 1966, vol. 37, pp. 254-57.
27. B. Chalmers: *Liquids: Structures, Properties, Solid Interactions*, 1st ed., Elsevier, Amsterdam, the Netherlands, 1965.
28. G.M. Swallowe, J.E. Field, C.S. Rees, and A. Duckworth: *Acta Mater.*, 1989, vol. 37, pp. 961-67.
29. R. Chow, R. Blindt, R. Chivers and M. Povey: *Ultrasonics*, 2005, vol. 43, pp. 227-30.
30. D. Shu, B. Sun, J. Mi and P.S. Grant: *Metall. Mater. Trans. A*, 2012, vol. 43, pp. 3755-66.
31. Y. Wang, X. Liu, K.S. Im, W. K. Lee, J. Wang, K. Fezzaa, D. S. Hung and J. R. Winkelman: *Nat. Phys.*, 2008, vol. 4, pp. 305-09.
32. K. Fezzaa, Y. Wang: *Phys. Rev. Lett.*, 2008, vol. 100, pp. 13-16
33. R. Boll, D. Anielski, C. Bostedt, J. Bozek, L. Christensen, R. Coffee, S. De, P. Decleva, S. Epp, B. Erk, L. Foucar, F. Krasniqi, J. Küpper, A. Rouzée, B. Rudek, A. Rudenko, S. Schorb, H. Stapelfeldt, M. Stener, S. Stern, S. Teichert, S. Trippel, M. Vrakking, J. Ullrich, and D. Rolles: *Phys. Rev. A*, 2013, vol. 88, no. 6, pp. 1402-1406
34. D. Milathianaki, S. Boutet, G. J. Williams, A. Higginbotham, D. Ratner, A. E. Gleason, M. Messerschmidt, M. M. Seibert, D. C. Swift, P. Hering, J. Robinson, W. E. White, and J. S. Wark: *Science*, 2013, vol. 342, pp. 220-23.
35. T. B. Massalski, and H. Okamoto: *Binary Alloy Phase Diagrams*, 2nd ed., Materials Park, ASM International, USA, 1990.

36. J. Vizdal, M. H. Braga, A. Kroupa, K. W. Richter, D. Soares, L. F. Malheiros, and J. Ferreira: *Calphad*, 2007, vol. 31, pp. 438-48.
37. M. Drakopoulos: <http://www.diamond.ac.uk/Beamlines/Engineering-and-Environment/I12/applications.html>.
38. R.C. Gonzalez, R.E. Woods and S.L. Eddins: *Digital Image Processing Using MATLAB*, 2nd ed., Gatesmark, LLC, USA, 2009.
39. Y. A. Hassan and R. E. Canaan: *Exp. Fluids*, 1991, vol. 12, pp. 49-60.

Figures

Fig 1.

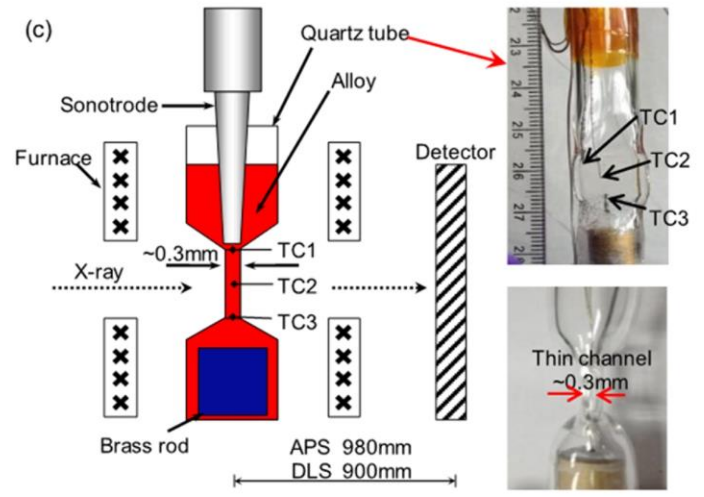
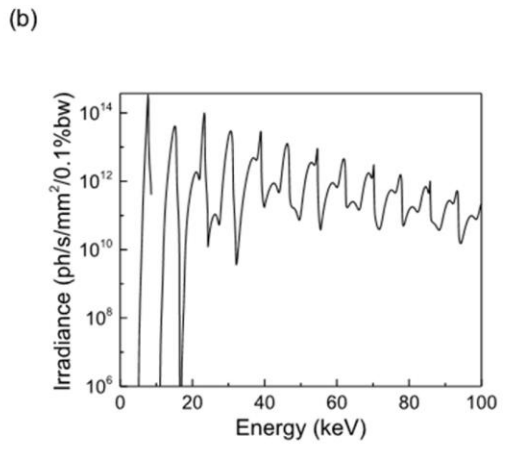
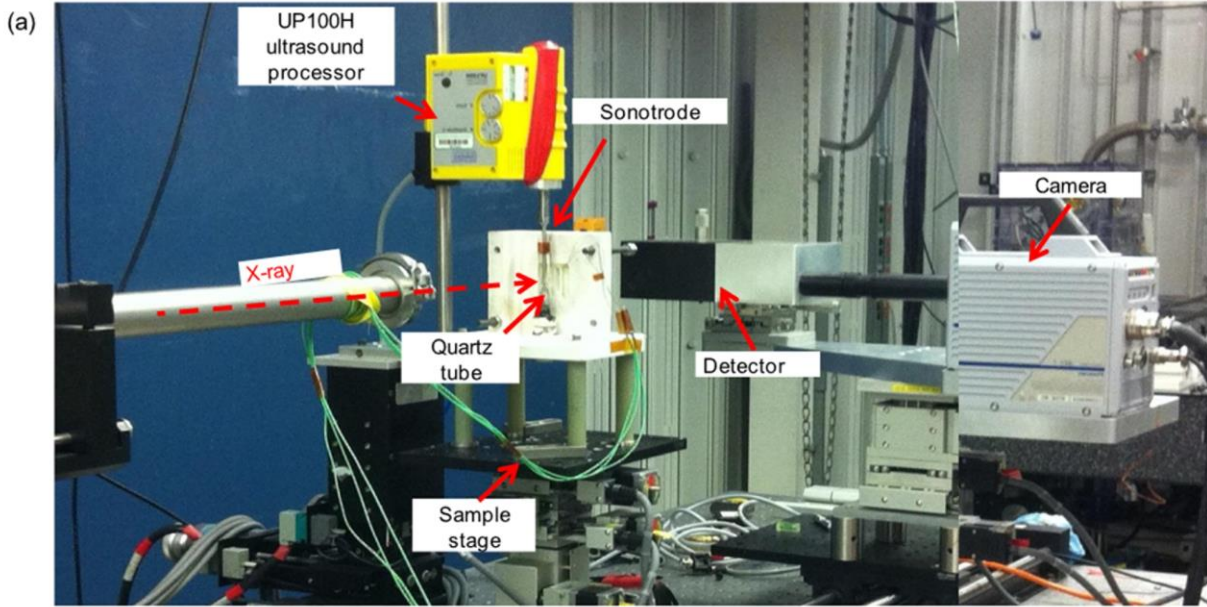


Fig 2.

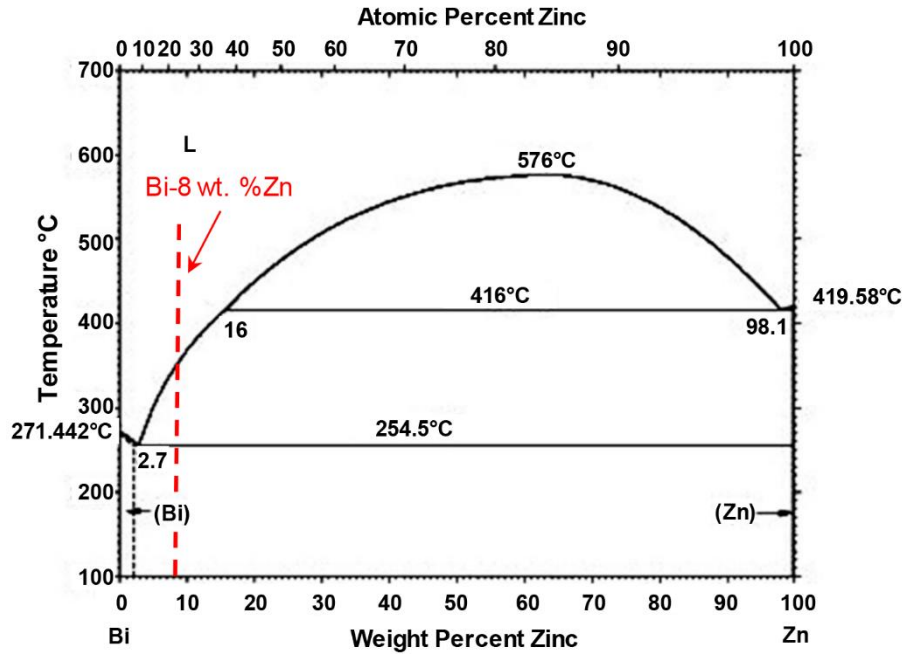


Fig 3.

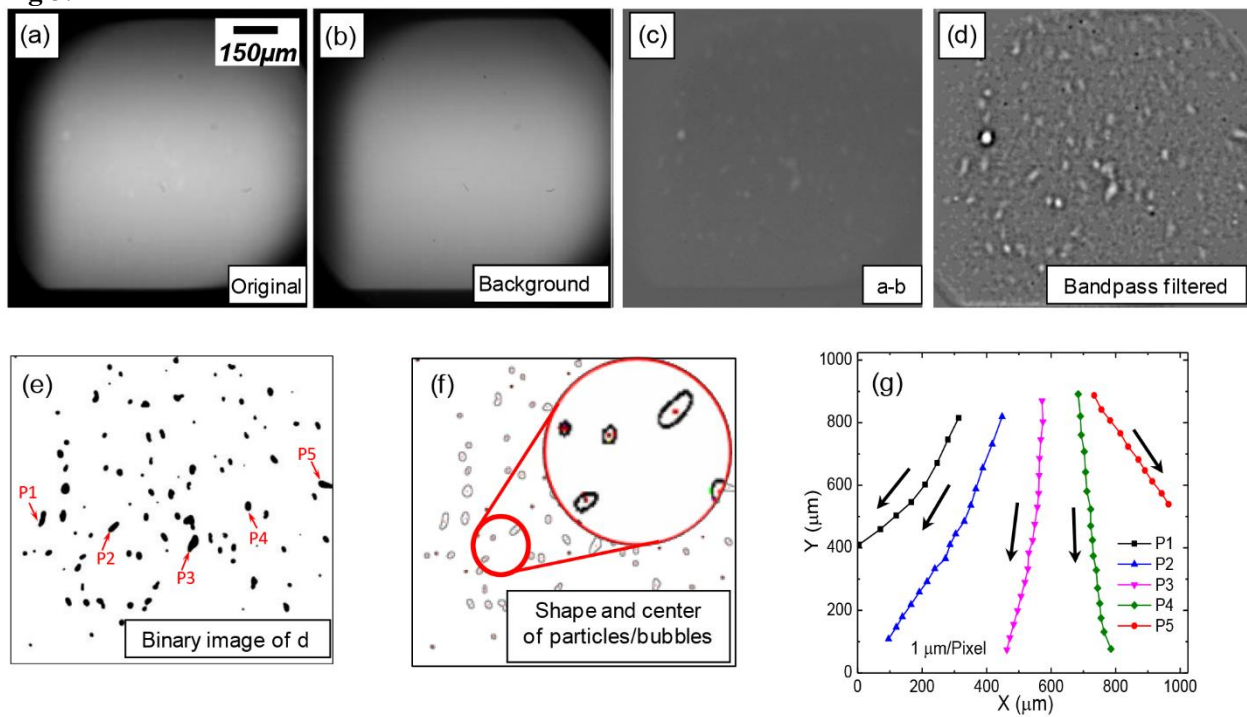


Fig 4.

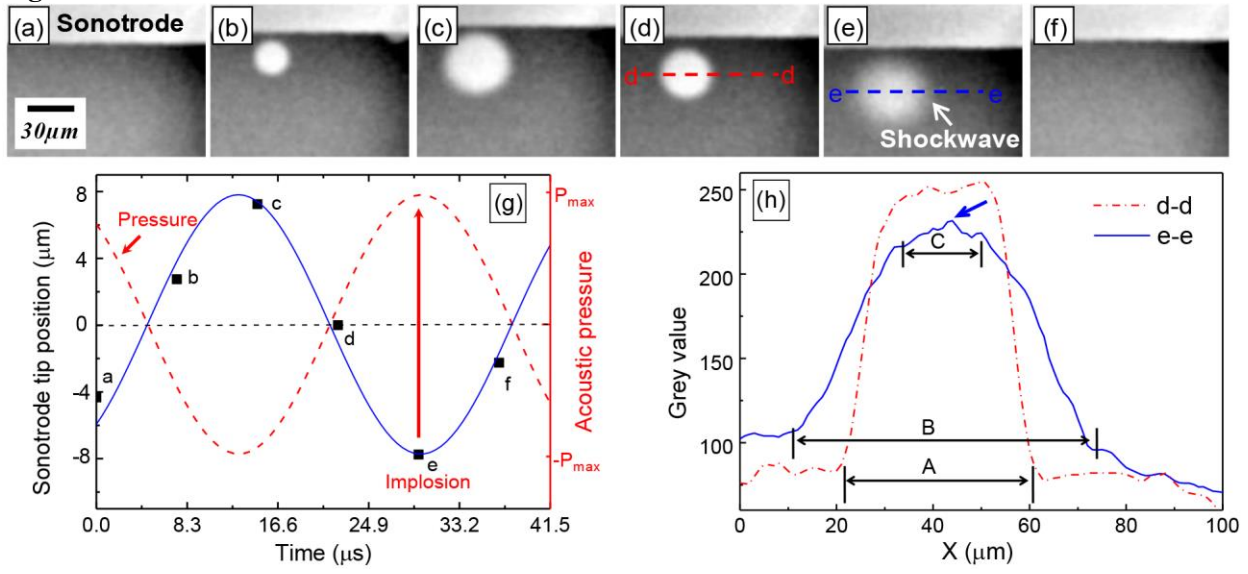


Fig 5.

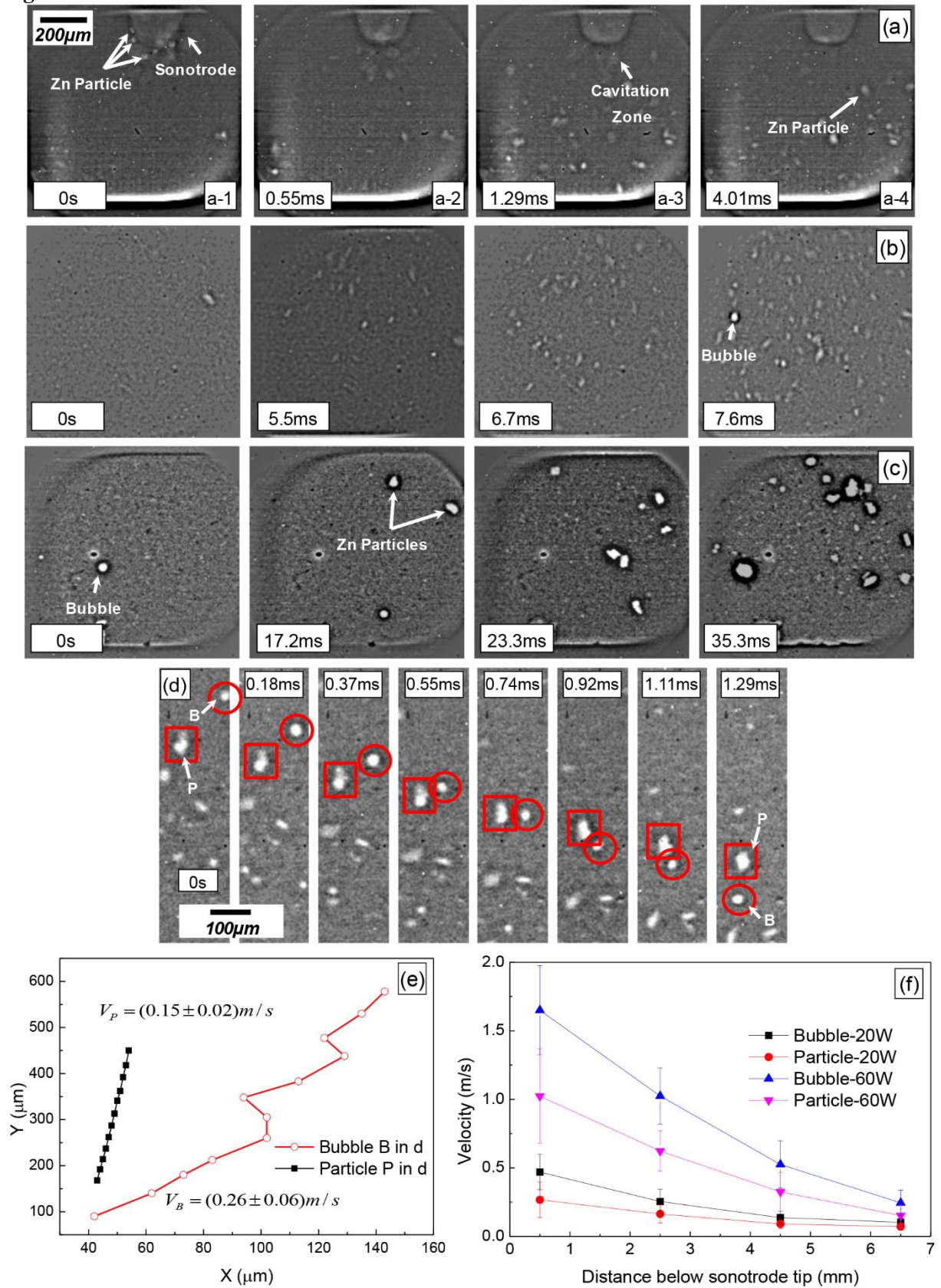
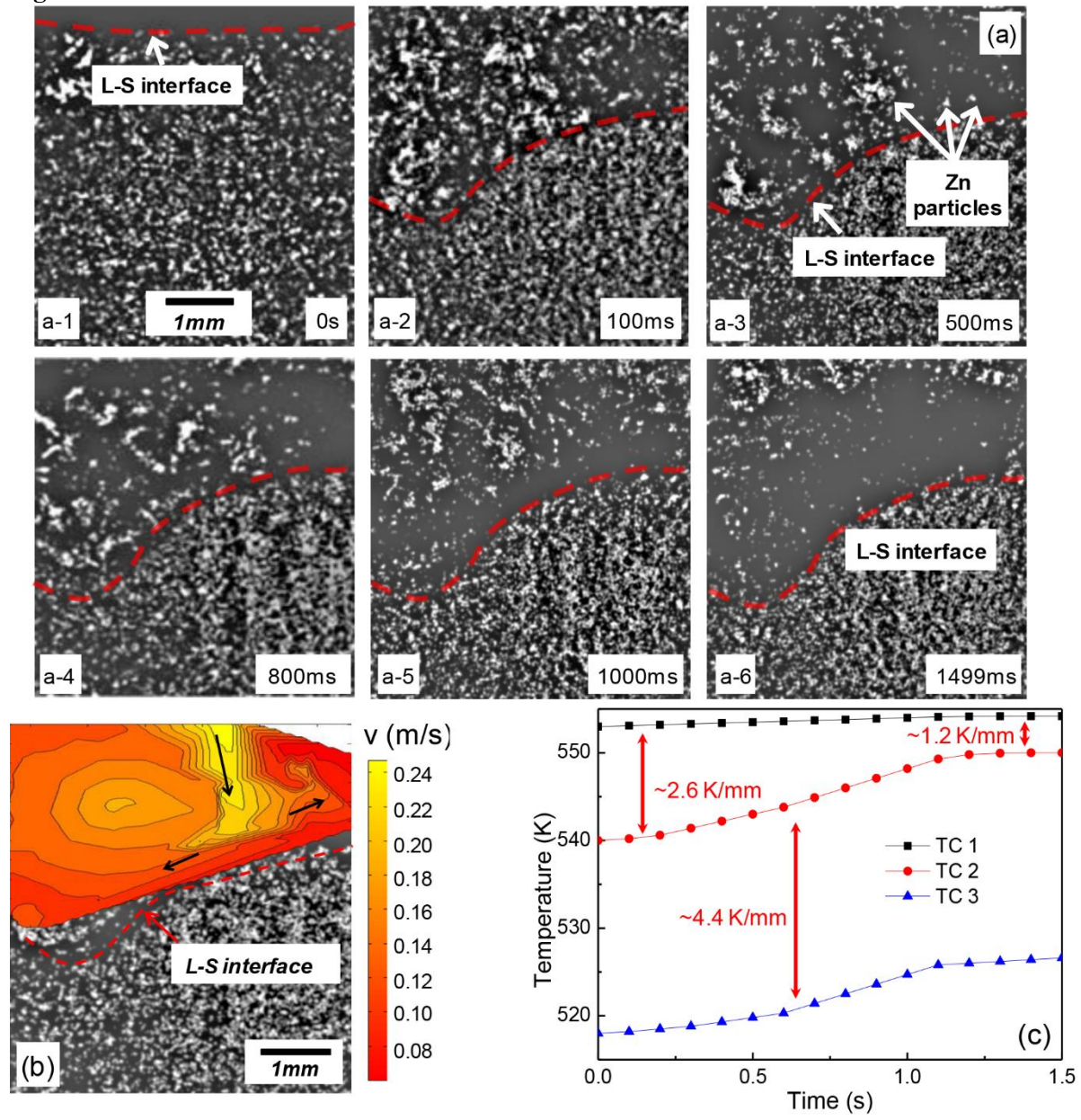


Fig 6.



List of figure captions:

Fig. 1: (a) A photo, showing the experimental set-up at 32-ID-B of APS. (b) The X-ray energy spectrum at 18mm undulator gap on a logarithmic scale, and (c) a schematic (left) and two photos (right), highlighting the purposely-made quartz tube with a $\sim 300 \mu\text{m}$ thin channel in the middle for X-ray imaging. Three K-type thermocouples (TC1, TC2, and TC3) were inserted inside the thin channel to measure the temperatures of the metal alloys, and a sonotrode was placed at the wedge area above the thin channel to transmit ultrasonic waves into the metal held inside the thin channel.

Fig. 2: The Bi-Zn binary phase diagram [35, 36] with the dash line marking the Bi - 8wt%Zn alloy used in the experiment.

Fig. 3. (a) A typical raw X-ray image acquired at APS using 5413 fps, (b) a typical background image acquired from a pure liquid Bi – 8 wt. %Zn, (c) the image obtained by subtracting b from a, (d) the image after applying the band-pass filter on c, (e) the binarised image of d, (f) the shape profiles and centroids of the particles and bubbles, and (g) the trajectory of five typical particles for the image sequence acquired at 2.5mm below the sonotrode tip using an ultrasound input power of 20W. The arrows indicate the direction of movement.

Fig. 4: (a) - (f) The six consecutive images, showing the oscillation and implosion of a bubble in a single wave period (an exposure time of 500 ns, and a time interval of $7.4 \mu\text{s}$ between the consecutive images), (g) the positions of the sonotrode tip that are measured from images (a) to (f) and superimposed onto the sine wave of the ultrasound, and the corresponding alternating acoustic pressure; and (h) the distributions of the grey levels along the dashed lines in (d) and (e), A is the diameter of the bubble in (d) and B is the diameter of the white halo in (e).

Fig. 5. A series of images captured in liquid Bi-8 wt. %Zn alloy with an ultrasound power of 20 W at APS using 5413 fps. The images were taken at (a) 0.5 mm, (b) 2.5 mm, and (c) 4.5 mm respectively below the sonotrode tip. (d) Eight typical images extracted from the image sequence showed in (b), showing the locations of bubble B and particle P, and their trajectories were plotted in (e). (f) The velocities of particles and bubbles at different distances away from the sonotrode tip when the ultrasound input powers of 20 W and 60 W applied. The error bar is the

standard deviation of the measured dataset (> 20 particles and bubbles are measured for each point) in the field of view.

Fig. 6: (a) Images of ultrasound enhanced fluid flow disrupting the structure of semisolid phase and leading to the detachment of Zn particles (1500 fps, 660 ms exposure time, and 60 W ultrasound power applied by 1 s, 2 mm tip diameter sonotrode), the center of the image is ~4.5 mm below the sonotrode tip. (b) Velocity contour of fluid flow above the L-S interface measured by tracking the detached Zn particles, and (c) the temperature history after the ultrasound was switched on. (All the images are captured at I12 DLS)